Journal of Colloid and Interface Science 513 (2018) 231–239

Contents lists available at ScienceDirect

Journal of Colloid and Interface Science

journal homepage: www.elsevier.com/locate/jcis

Regular Article

Biomass-derived porous carbon modified glass fiber separator as polysulfide reservoir for Li-S batteries

Ramakrishnan Kalai Selvan [a,b,1], Pei Zhu [a,1], Chaoi Yan [a], Jiadeng Zhu [a,c], Mahmut Dirican [a], A. Shanmugavani [b], Yun Sung Lee [d], Xiangwu Zhang [a,*]

[a] Department of Textile Engineering, Chemistry and Science, North Carolina State University, Raleigh, NC 27695-8301, USA
[b] Energy Storage and Conversion Devices Laboratory, Department of Physics, Bharathiar University, Coimbatore 641-046, Tamil Nadu, India
[c] Department of Forest Biomaterials, North Carolina State University, Raleigh, NC 27695-8005, USA
[d] Faculty of Applied Chemical Engineering, Chonnam National University, Gwangju 500-757, South Korea

GRAPHICAL ABSTRACT

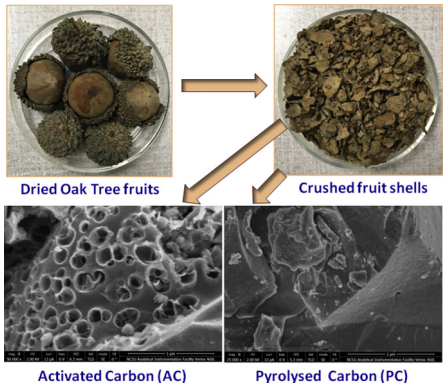

ARTICLE INFO

Article history:
Received 19 September 2017
Accepted 6 November 2017
Available online 7 November 2017

Keywords:
Biomass
Carbon, polysulfide
Energy storage
Li-S batteries

ABSTRACT

Biomass-derived porous carbon has been considered as a promising sulfur host material for lithium-sulfur batteries because of its high conductive nature and large porosity. The present study explored biomass-derived porous carbon as polysulfide reservoir to modify the surface of glass fiber (GF) separator. Two different carbons were prepared from Oak Tree fruit shells by carbonization with and without KOH activation. The KOH activated porous carbon (AC) provides a much higher surface area (796 $m^2 g^{-1}$) than pyrolized carbon (PC) (334 $m^2 g^{-1}$). The *R* factor value, calculated from the X-ray diffraction pattern, revealed that the activated porous carbon contains more single-layer sheets with a lower degree of graphitization. Raman spectra also confirmed the presence of sp^3-hybridized carbon in the activated carbon structure. The C—OH functional group was identified through X-ray photoelectron spectroscopy for the polysulfide capture. Simple and straightforward coating of biomass-derived porous carbon onto the GF separator led to an improved electrochemical performance in Li-S cells. The Li-S cell assembled with porous carbon modified GF separator (ACGF) demonstrated an initial capacity of 1324 mAh g^{-1} at 0.2 C, which was 875 mAh g^{-1} for uncoated GF separator (calculated based on the 2nd cycle). Charge

* Corresponding author.
E-mail address: xzhang13@ncsu.edu (X. Zhang).
[1] The first two authors equally contributed to this work.

https://doi.org/10.1016/j.jcis.2017.11.016

transfer resistance (R_{ct}) values further confirmed the high ionic conductivity nature of porous carbon modified separators. Overall, the biomass-derived activated porous carbon can be considered as a promising alternative material for the polysulfide inhibition in Li–S batteries.

1. Introduction

Lithium-sulfur (Li-S) batteries have been considered as one of the most promising energy storage systems for the emerging electric vehicles and hybrid electric vehicles due to their high specific capacity (1675 mAh g^{-1}) and large energy density (2500 Wh kg^{-1}) [1]. Meanwhile, sulfur is environmentally benign and economically viable because of its low cost. However, commercialization of Li-S batteries is mainly hindered by the dissolution of polysulfides, which reduces the sulfur content in cathode during cycling, leading to serious capacity fading [2–4]. So far, many attempts have been made to prevent the diffusion of polysulfides by using various carbonaceous materials including porous carbons, graphene, reduced graphene oxide (rGO), carbon nanotubes (CNTs) and activated carbon as the sulfur cathode hosts [5–9]. The use of these carbonaceous materials improved active material utilization and cell cyclability because they act as the conductive frameworks to enhance the electrical conductivity of the cathodes and reduce the loss of soluble polysulfide intermediates during the cycling. However, the use of these carbonaceous hosts to host sulfur in the cathodes often involve complex structural designs and high costs, which limit their use in Li-S batteries. Hence, it is necessary to find a simple, scalable and cost -effective strategy to achieve high performance for Li-S batteries.

The surface modification of separators by coating different materials is an alternative and simple approach to address the polysulfide diffusion problem [10–12]. It is well known that separator plays an important role in preventing the battery from electrical short circuit while providing effective pathways for ion transportation between the electrodes [7,13,14]. Therefore, an ideal separator for Li-S batteries should have a good ionic conductivity after absorbing the liquid electrolyte and should be capable of trapping the soluble polysulfides during cycling. Different materials like poly(3,4-ethylenedioxythiophene), polystyrene sulfonate, Nafion, polyethylene glycol, polyaniline nanofibers, multiwalled carbon nanotubes (MWCNT), black phosphorus [15–19], activated porous carbon tubes, graphene, etc. [20–22] have been used as separator surface-modifiers to suppress the shuttling of polysulfides and to preserve the active materials for maintaining the cycling stability of the Li-S cells. Wang et al. [23] prepared a hybrid separator by coating glass fibers onto microporous Celgard polypropylene (PP) membrane with a layer, and the resultant Li-S cell achieved a capacity of 1010 mAh g^{-1} at 0.5 C. Wang et al. [24] also used a multi-walled carbon nanotube@polyethylene glycol (MWCNT@PEG) composite to modify the commercial Celgard separator. The Li-S cell assembled with MWCNT@PEG composite-coated separator exhibited an initial discharge capacity of 1283 mAh g^{-1} at 0.5 C. Furthermore, Ketjen Black-MnO composite was synthesized and coated on a commercial separator Celgard 2400 and the resultant Li-S cell retrieved the capacity of 1200 mAh g^{-1} at 0.2 C [25]. In addition, hollow spherical cerium oxide particles were coated on commercial separator Celgard 2400 and delivered the capacity of 1004 mAh g^{-1} at 1 C [26]. Apart from the above-mentioned materials, coating biomass -derived carbons is one of the recent strategies to enhance the Li-S cell performance. Biomass-derived activated carbons have unique features of the such as high surface area, tunable pore structure, large pore volume and startling functional groups, which can be tailored by varying the preparation conditions [27–29]. As a result, researchers have shown immense interest to identify and explore various biomasses for the Li-S applications.

In the present work, Oak Tree fruit shells derived porous carbon coated glass fiber (GF) membrane separators are prepared and investigated their polysulfide trapping ability in Li-S cells. This biomass-derived porous carbon contains a large number of pores with different pore sizes and various functional groups, which are beneficial for capturing polysulfides in Li-S cells. GF membrane is used as the separator substrate for carbon coating because of its high porosity (65%), large electrolyte intake, superior thermal stability, easy availability and low cost, compared to microporous PP or polyethylene (PE) membrane separators [30,31]. Coating the biomass-derived porous carbon on GF membrane could effectively inhibit the diffusion of polysulfides. Electrochemical results revealed that biomass-derived activated carbon modified GF separators show good electrochemical performance by retarding the polysulfide shuttling and improve the sulfur utilization in the Li-S batteries. Li-S cells assembled with biomass-derived porous carbon modified GF separators demonstrated an initial capacity of 1324 mAh g^{-1} at 0.2 C, which was 875 mAh g^{-1} for uncoated GF separator, and provided ~80% capacity retention even after 50 cycles.

2. Experimental methods and materials

2.1. Porous carbon preparation and separator modification

The porous carbons were prepared from Oak Tree fruit shells as follows. Initially, the dried Oak Tree fruit shells were pulverized and washed with distilled water and dried under vacuum for overnight. Then the dried fruit shells were activated in 20% of KOH for 24 h. Subsequently, they were carbonized at 700 °C for 3 h under nitrogen atmosphere. Finally, the as-prepared KOH-activated carbon material was further washed with distilled water and 1 M HCl to neutralize the product, followed by drying at 70 °C for overnight. This KOH-activated carbon is denoted as AC. For comparison, carbon samples were also prepared without KOH activation, *i.e.*, pyrolyzed directly, which is denoted as pyrolyzed carbon (PC).

Carbon-modified GF membrane separators were prepared by coating the as-prepared carbon materials directly on to the surface of the GF membranes (GE healthcare). The coating process started with preparing slurries by mixing 70 wt% as-prepared carbon (PC or AC), 10 wt% carbon nanotube (CNT, BTY-175, Blue Nano Inc.,) 10 wt% conductive carbon (C65, TIMCAL Graphite & Carbon Ltd.) and 10 wt% polyvinylidene fluoride (PVDF, Solef® PVDF-5130, Solvay) in N-methyl-2-pyrrolidone (NMP, Sigma-Aldrich). The slurries were then coated onto the GF membranes by using the doctor blade casting method. Subsequently, the coated separators were dried under vacuum at 60 °C for overnight.

2.2. Electrode fabrication and cell assembly

The sulfur cathodes were fabricated by preparing a slurry of 70 wt% pure sulfur (Sigma-Aldrich), 20 wt% conductive carbon (TIMCAL, Graphite & Carbon Ltd., C-65), and 10 wt% PVDF in the desired amount of NMP, which was later coated on the carbon-coated aluminum foil by using doctor blade and followed by drying under

vacuum at 60 °C for overnight. The areal loading of sulfur for the as-prepared electrodes ranged between 0.80 and 1.1 mg cm^{-2}. For electrochemical testing, the 2032 type coin cells were assembled using the sulfur electrode, porous carbon modified GF separator and Li metal (Sigma-Aldrich) as the counter electrode. The electrolyte used was 1 M bis(trifluoromethane)sulfonamide lithium (LiTFSI, Sigma-Aldrich) and 0.1 M lithium nitrate (99.99% trace metals basis, Sigma-Aldrich) in a mixture of 1,3-dioxolane (DOL, Sigma-Aldrich) and 1,2-dimethoxyethane (DME, Sigma-Aldrich) (1: 1 by volume). The coin cell assembling was conducted in an argon-filled glove box and the cell capacity was calculated based on the sulfur mass.

2.3. Characterization techniques

Field emission scanning electron microscopy (FESEM, Quanta 3D FEI, USA) was used to identify the morphological features of the samples. Structural properties of the PC and AC were elucidated by using X-ray Diffraction patterns (Rigaku D/Max 2400 (Japan)) with Cu Kα radiation (λ = 1.5418 Å). Raman spectral analysis was carried out in LabRam HR800 UV Raman microscope (Horiba Jobin-Yvon, France), KBSI, Gwangju-center, Time-resolving PL/Raman spectrometer (Focal length; 80 cm, Excitation light source: 515 nm Diode laser and Applied laser power on the sample surface: 10% of 10 mW). BET surface area and pore size analysis of the samples were examined by using an ASAP 2020 instrument. X-ray photoelectron spectroscopy (XPS, SPECS FlexMod, Germany) was performed to identify the surface functional groups of the PC and AC by using a Kratos Analytical spectrometer and monochromatic Mg Kα X-ray source.

The cyclic voltammetry (CV) analysis was carried out by using Gamry reference 600 electrochemical workstation in a potential range of 2.8–1.7 V vs Li^+/Li with a scan rate of 0.1 mV s^{-1}. Electrochemical impedance spectroscopy data were also obtained using the same device in the frequency range between 0.1 m Hz and 1 M Hz with an AC voltage amplitude of 5 mV. Cycling performances of the Li-S cells were tested with Arbin battery tester in a potential range of 1.7–2.8 V.

3. Results and discussion

3.1. Morphology and structural characterization

Fig. 1(a, b) represents the photographic images of the Oak Tree fruit shells. Fig. 1(c, d) shows the FESEM images of the PC and AC samples. It is seen that PC exhibited uniform surface without any observable pores. As well as it looks like solid graphitic carbon since it was not activated by KOH. On the other hand, AC had a rough surface with channel-like open pores, which were in the nanoscale range. These pores are very useful for improving the specific surface area thereby increasing the polysulfide capturing capability through the surface functional groups. Fig. 1(e, f) shows the FESEM images of the cross-sectional view of PC and AC coated GF separators. It is seen that the thickness of the AC coated separators is are almost uniform throughout the area. On the other hand, the PC coated separators are not uniform even though the same methodology has been adopted for the coating process. This may be due to the larger particle size of PC since the samples are not activated.

X-ray diffraction patterns of PC and AC are demonstrated in Fig. 2. PC presented a broad amorphous peak centered at $2\theta = 23^\circ$ corresponding to the (0 0 2) diffraction plane, which was attributed to the turbo-static nature of carbon [32]. Interestingly, for AC, this diffraction plane was shifted to a lower angle ($2\theta = 19^\circ$). This result indicated the formation of the small disordered structure of aromatic sheets or disordered carbon due to the chemical activation effect [33]. On the other hand, both PC and AC had a broad peak at $2\theta = 43^\circ$ corresponding to the (1 0 0) diffraction plane, which was an indication for the occurrence of small graphene sheets [34]. Calculated d-spacings of PC and AC were 3.64 Å and 4.48 Å, respectively, which were higher than that of graphite (3.35 Å) [35]. Larger d-spacing of AC was ascribed to the expansion of single layer content, which in turn for the formation of porous structure. To measure the content of single layer carbon sheets, empirical parameter R-value was calculated based on the formula introduced by Dahn et. al., [36,37]. The R-factor is the ratio between the height of (0 0 2) plane Bragg's diffraction peak to its background. Calculated R values of PC and AC were 2.157 and 1.479, respectively. Lower R-value of AC proved that it contains more single-layer graphene sheets with a lower degree of graphitization due to the chemical activation [38]. On the other hand, the high R-value of PC indicated that it had a high concentration of graphene sheets stacked one by one like graphite without any significant pores.

Fig. 3 shows the Raman spectra of PC and AC. Both PC and AC exhibited two characteristic peaks at around 1340 and 1600 cm^{-1}, corresponding to D- and G-band, respectively. The D-band mainly arises due to out of plane vibration of A_{1g} corresponding to the structural defects, edge defects and dangling sp^3 bond (diamond-like carbon) of disordered carbon [39]. It is also associated with the breathing oscillation of full six-member carbon rings. On the other hand, the G-band is ascribed to the in-plane vibration mode of E_{2g} in sp^2 carbon (graphite-like carbon) [40]. Comparatively, the intensity of G-band was higher for PC due to the highly graphitic nature. However, the lower degree of graphitization was obtained for AC, which was due to the separation of the individual graphene-like sheets. This result confirmed the XRD analysis data. To further determine the insight of defects in the as-prepared carbon structure, the intensity ratio (I_D/I_G) was calculated by employing the maximum peak intensities of D and G bands. It is noticed that the I_D/I_G ratio increased from 0.853 to 0.901 after activation, which elucidated the formation of more sp^3 hybridized carbon bonds. This might be related to the increased number surface functional groups formed after activation, which is useful for the adsorption of polysulfides [41].

Fig. 4a shows the N_2 adsorption-desorption isotherms of PC and AC samples. It reveals that PC shows type IV(b) isotherm with H4 hysteresis loop. Calculated BET specific surface area of PC was 333.7 m^2/g. On the other hand, AC exhibited Type IV(a) isotherm with H4 hysteresis loop, which indicated the existence of majority mesopores and a few micropores [42]. Observed hysteresis loop at the medium pressure (P/P_o = 0.4–0.9) was the evidence for the presence of mesopores. The slope at very low pressure (0–0.2) was related to the formation of micropores and a small tail-like behaviour in the isotherm at nearly 1.0 (>0.9) indicated the macropores region [43]. Calculated BET specific surface area of AC was 795.8 m^2/g. These results revealed that the specific surface area was significantly increased after activation using KOH.

Pore size distribution (Fig. 4b) was obtained through the Barrett–Joyner–Halenda (BJH) method [44]. High-intensity peaks over 2 nm and small peaks around 24 and 43 nm were indexed for the AC, which further confirmed the presence of mesopores. Formation of macropores was confirmed by the peak indexed at 76 nm. At a very low relative pressure, the steep intake of gases demonstrated the presence of open pores in AC [45]. These results are consistent with the SEM observation (Fig. 1), since the SEM images clearly exhibited that the pores were continuous and had bundle-like structure [46]. On the other hand, no significant peaks were obtained for PC in the 2–50 nm range except over 2 nm. Similarly, the calculated total pore volume of AC (0.3772 cm^3/g) was higher than that of PC (0.1526 cm^3/g). Normally, this improved pore vol-

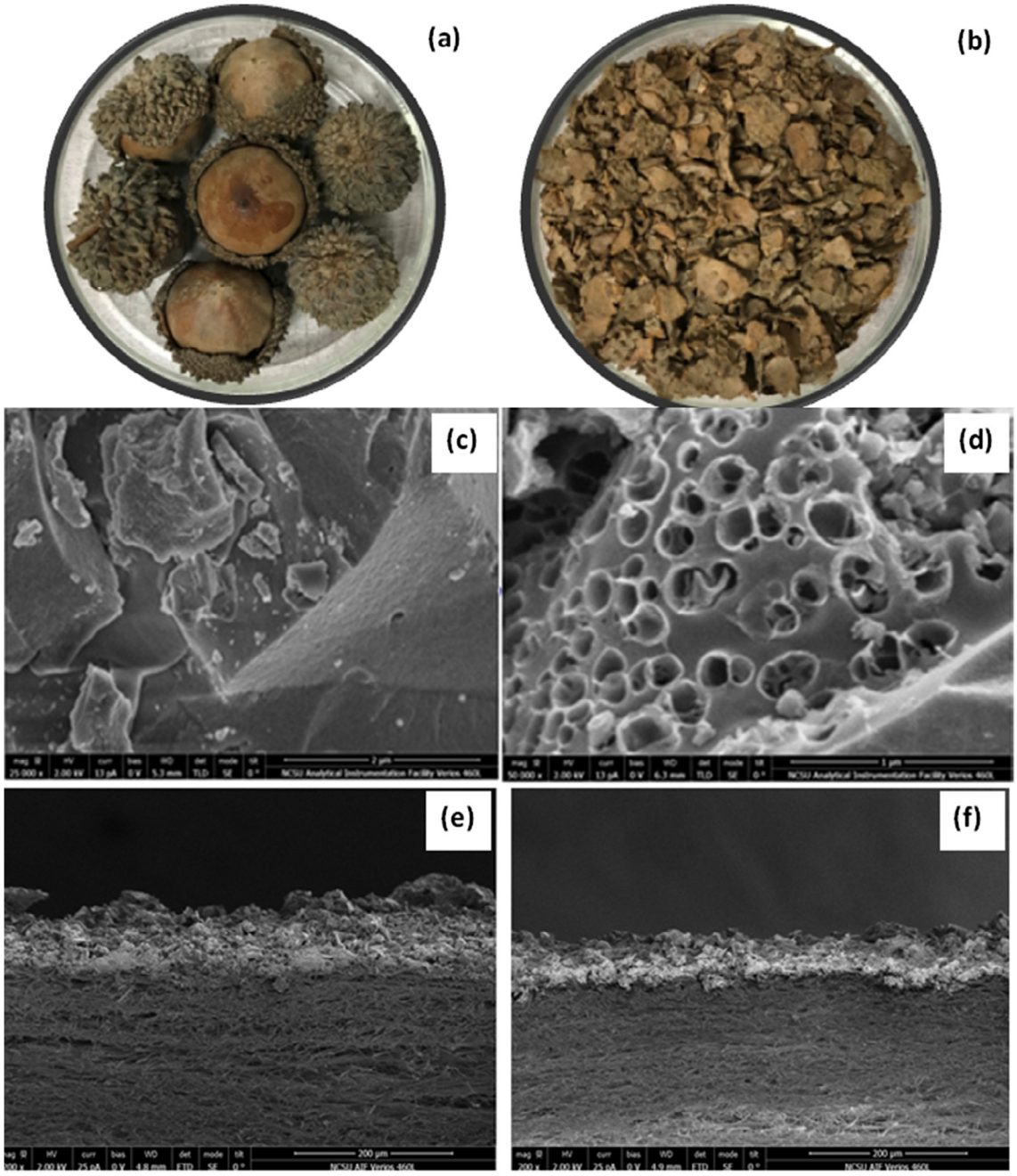

Fig. 1. Photographic images of (a) Oak tree fruit cells and (b) crushed fruit cells. FESEM images of (c) pyrolyzed carbon and (d) activated carbon. FESEM images of the cross-sectional view of (e) pyrolyzed carbon and (f) activated carbon coated GF separators.

ume is more favorable for the electrochemical reaction because it easily the insertion and de-insertion of the electrolyte ions in the materials [47]. The increased average pore diameter of AC (1.896 nm), when compared with PC (1.8289 nm) will also favourably contribute to the electrochemical reaction. Observed saturated adsorbed volume with respect to pore width (inset Fig. 4b) further substantiates the high surface area of AC [47].

Surface elemental compositions of PC and AC were identified through XPS spectra and the results are shown in Fig. 5. Survey spectrum of PC (Fig. 5a) showed two prominent peaks at a binding energy of 284.55 and 533.06 eV, respectively, which were attributed to the presence of C 1s (Fig. 5b) and O 1s (Fig. 5c). Deconvoluted C 1s peak with a binding energy of 284.6, 286.15, 287.62, and 289.38 eV inferred to the presence of functional groups of C═C/C—C, C—OH or sp^3 carbon, C═O, and O═C—OH, respectively [33,48]. Furthermore, prominent O 1s was deconvoluted into five peaks at a binding energy of 533.38, 534.89, 532.21, 531.05 and 536.39 eV, indicating the presence of hydroxyl group (C—OH) in phenol or C—O bond, O—C═O, (C—OH) hydroxyl group, C═O (carboxyl group), and chemisorbed water, respectively [33,48]. Additionally, the obtained atomic percentages of various elements were 46.64 At.% C 1s, 40.89 At.% O 1s, and 12.48 At.% B 1s. Similarly, the survey spectrum of AC also exhibited two prominent peaks at 284.71 eV (C 1s) and 533.50 eV (O 1s) (Fig. 5d). Here, C 1s was deconvoluted into three peaks at a binding energy of 284.6, 285.98 and 288.61 eV, corresponding to the C═C/C—C, C—OH (hydroxyl group) and O═C—OH, respectively (Fig. 5e). O 1s was deconvoluted into four peaks at a binding energy of 532.65,

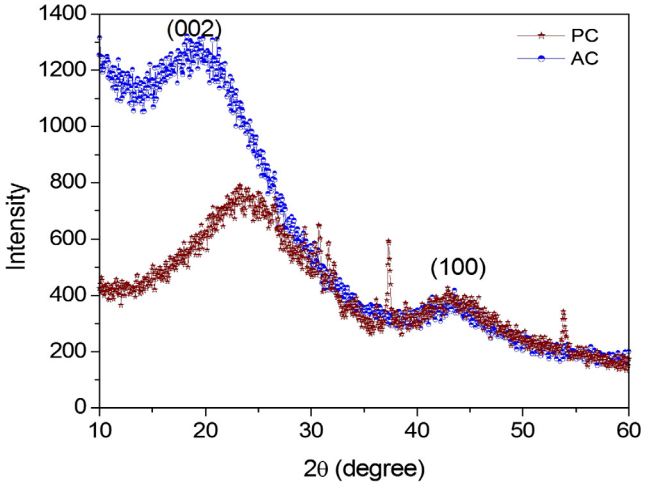

Fig. 2. XRD patterns of PC and AC samples.

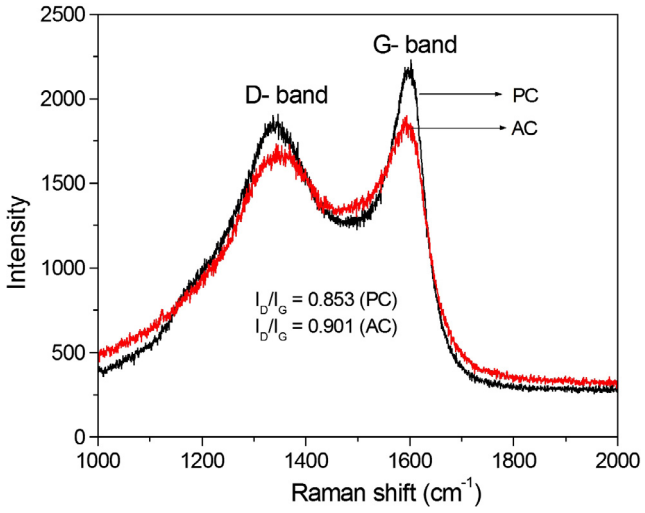

Fig. 3. Raman spectra of PC and AC samples.

531.57, 533.6 and 535.71 eV, which revealed the presence of C—OH (hydroxyl group), carbonyl/quinine group (C=O), hydroxyl groups C—OH, in phenol or C—O groups and chemisorbed water, respectively (Fig. 5f). Corresponding elemental compositions were found to be 79.48 At.% C 1s, and 18.39 At.% O 1s. These results confirmed that C 1s/O 1s ratio increased from 1.1 to 4.3 after activation. This might be due to the formation of more single-layer carbon sheets with a low degree of graphitization, which was also revealed by the calculated R-value from XRD analysis. Further, the presence of functional groups effectively contributes to trapping the polysulfides from shuttling due to the electrostatic force between the oxygen-containing groups and the negatively charged polysulfides. As a result, it is believed that AC was more effective for polysulfide trapping. In addition, the porous structure of AC might benefit the electrolyte permeation and ion/electron transfer, which could enhance the electrochemical performance of the Li -S cells [33,48].

3.2. Electrochemical performance analysis

Cyclic voltammetry (CV) analysis was performed to investigate the electrochemical performance of the fabricated Li-S cells using the separators of GF (GF cell), PC coated GF (PCGF cell), and AC coated GF (ACGF cell) in the potential range between 1.7 and 2.8 V vs Li^+/Li at a scan rate of 0.1 mV s^{-1}. The first five consecutive cycles of all the cells are demonstrated in Fig. 6a–c. In the first cycle of GF cell (Fig. 6a), two prominent cathodic peaks and one anodic peak were observed. The anodic peak observed at 2.50 V vs Li/Li^+ was attributed to the oxidation of short-chain polysulfides to L_2S_8 [10]. Subsequently, the first reduction peak at around 2.13 V vs Li/Li^+ was due to the fast-kinetic reduction of sulfur to soluble long-chain polysulfides (Li_2S_x, $4 \leq x \leq 8$), whereas the second cathodic peak at around 1.99 V vs Li/Li^+ was caused by the slow kinetic process related to the reduction of insoluble short-chain lithium sulfides (Li_2S_2, Li_2S) [10]. On increasing cycle from 2 to 5, a shift in anodic peak potential is noticed. At the 5th cycle, the anodic peak is seen at around 2.47 V and the first and second cathodic peak appear at around 2.23 V and 2.0 V, respectively. It shows that in increasing cycles, the redox reaction tended to obtain its stable potential.

On the other hand, the anodic peak of the first cycle was observed at around 2.43 V for PCGF cell. Similarly, the first and second cathodic peaks were observed at around 2.16 V and 2.01 V. Whereas on increasing the cycle from 2 to 5, the anodic peak remains in the potential 2.43 V. However, the first and second cathodic peak shifted to 2.26 V and 2.03 V, respectively. This observed slight shift in the cathodic peaks toward positive potential might be due to the rearrangement of migrating active material to their electrochemically favorable positions in PCGF Li-S cells [49].

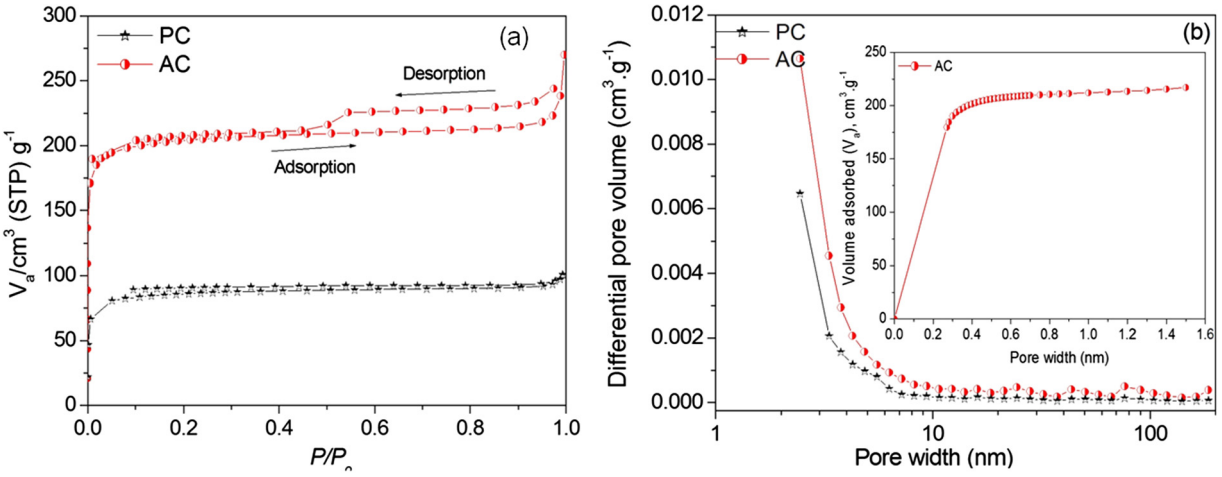

Fig. 4. N_2 adsorption and desorption isotherms (a) and pore structure distribution (b) of PC and AC (Inset: pore width vs volume adsorbed curve of AC).

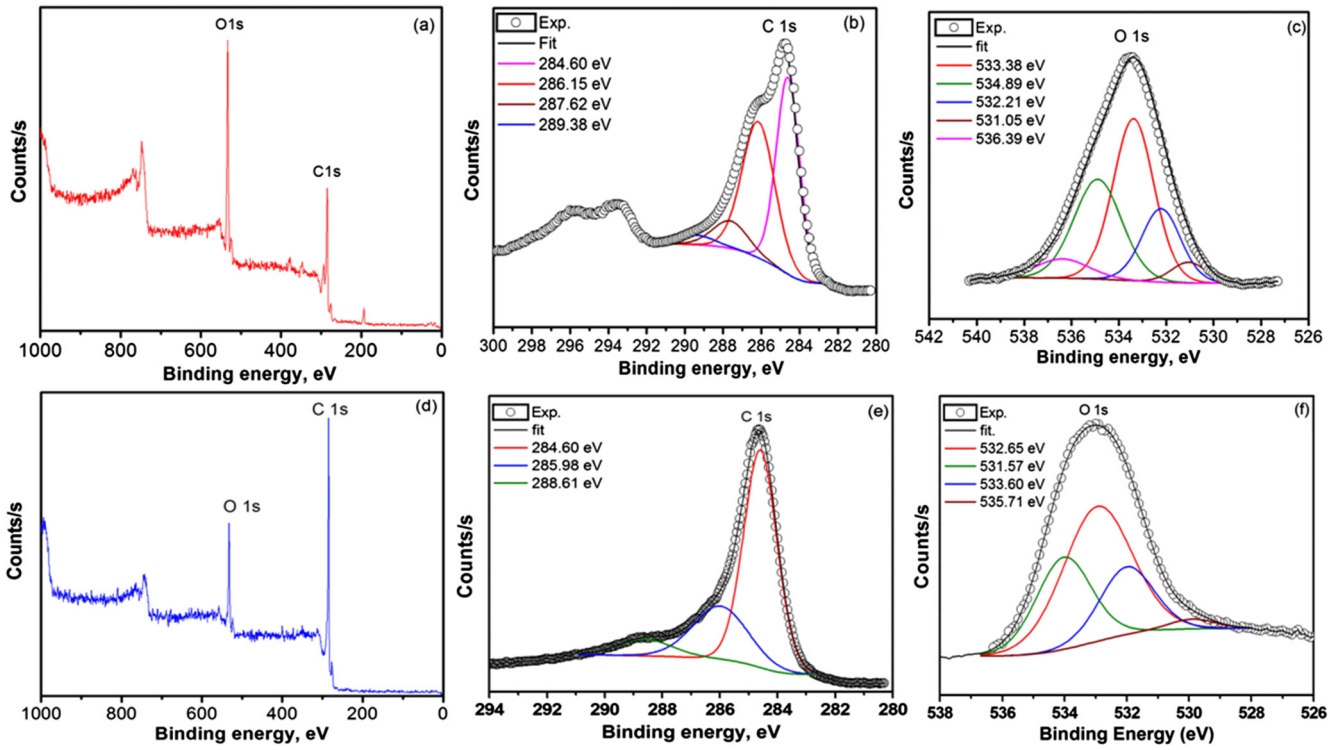

Fig. 5. XPS survey spectra (a, d), deconvoluted C 1s (b, e) and O 1s (c, f) of PC and AC, respectively.

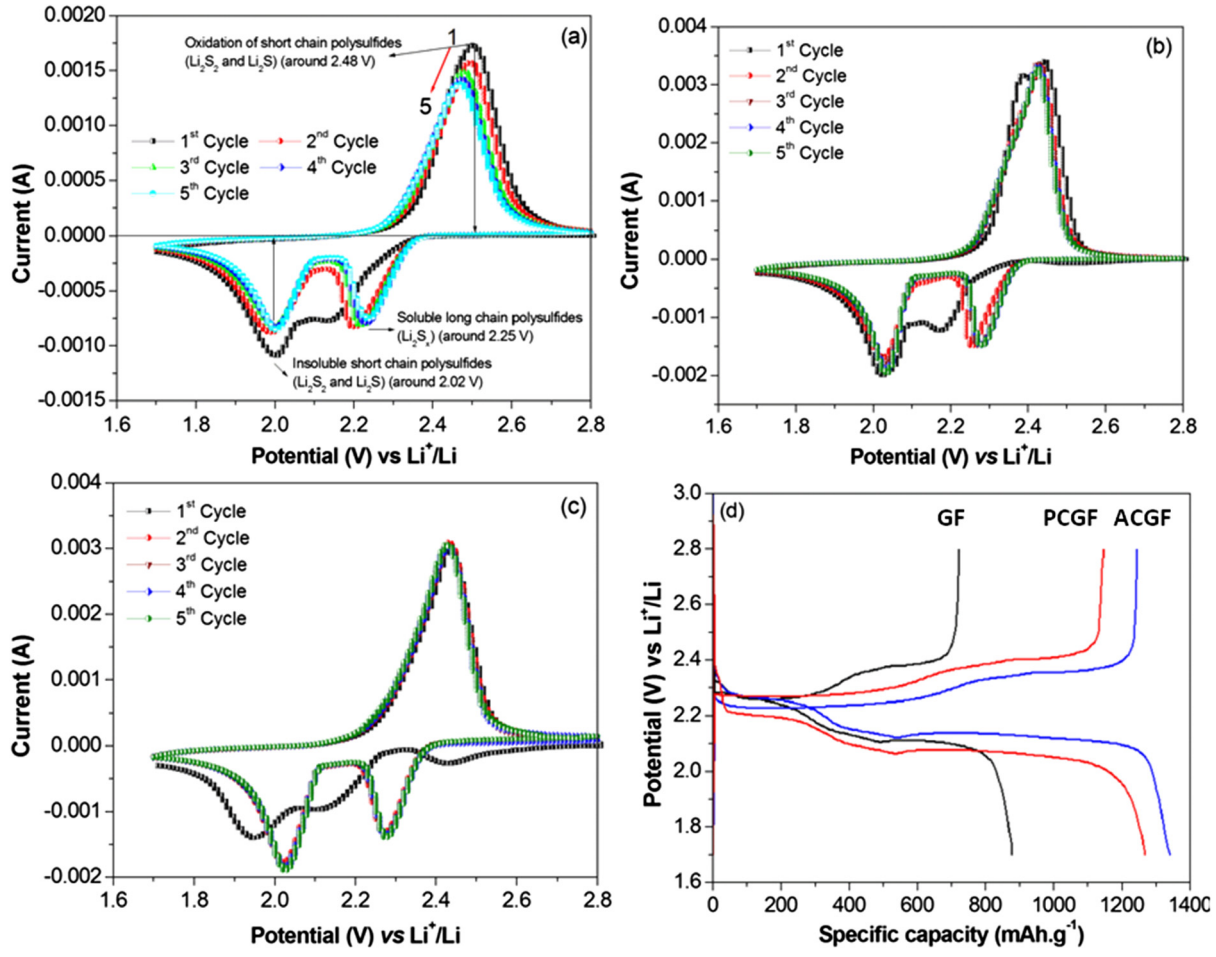

Fig. 6. CV curves of the Li-S cells with (a) GF, (b) PCGF, and (c) ACGF. (d) Typical 1st discharge/charge curves of the Li-S cells at 0.2 C.

Interestingly, a sharp anodic peak was noticed at around 2.43 V in the first cycle of ACGF cells. As well as three reduction peaks were obtained at 2.43, 2.12 and 1.94 V. In the subsequent cycles, there is an occurrence of only two stable reduction peaks at around ~2.26 V and 2.02 V vs Li/Li^+. It was due to the activation effect in the ACGF based cells for the conversion of the elemental sulfur process. The further sharpness of redox peaks on the subsequent cycles indicates the enhancement in the reaction kinetics caused by the better electrical conductivity and porous nature of the AC surface modified GF separators. Redox peaks sustaining their shape and position during the following cycles demonstrating the better reversibility of ACGF cells [50]. Overall, compared to GF cell, an increase in current area was noted for the PCGF and ACGF cells, which reveals the increase in capacity, high stability and fast redox process. Among these two, ACGF cell exhibits improved cycling stability due to the excellent overlapping of redox peaks through the strong polysulfides adsorption [51].

To further investigate the electrochemical performance of the GF, PCGF and ACGF cells, galvanostatic discharge/charge cycling tests were performed in the voltage range between 1.7 and 2.8 V vs Li^+/Li. Typical 1st discharge/charge curves of the Li-S cells at 0.2 C are shown in Fig. 6d. On the first discharge, two voltage plateaus at around 2.26 and 2.10 V were observed for all Li-S cells, corresponding to the reduction of sulfur into soluble, long chain polysulfides (Li_2S_x, $4 \leq x \leq 8$) and the formation of insoluble Li_2S_2/Li_2S, respectively [52]. During charging, one voltage plateau was observed at around 2.37 V for GF based Li-S cell. On the other hand, two voltage plateaus were determined at 2.28 and 2.40 V for PCGF cell, while similar voltage plateaus were observed at 2.24 and 2.35 V for ACGF cell. All those voltage plateaus appeared during the first cycle charging were ascribed to the oxidation reaction from lithium sulfides to polysulfides and finally to sulfur. Furthermore, the polarization potentials of the GF, PCGF and ACGF cells were 198, 178, and 71 mV, respectively. Lower over-potential of ACGF cell indicated its better reversibility resulted in trapping polysulfides during discharging.

Rate capability is a key parameter for Li-S batteries in high power applications. Fig. 7a–c shows typical discharge/charge profiles of the GF, PCGF and ACGF cells at various C-rates (0.2, 0.25, 1, and 1.5 C). Similarly, the rate capability of three different cells was further demonstrated by increasing the discharge/charge current density stepwise from 0.2 to 1.5 C every 10 cycles and the results are shown in Fig. 7d. Two plateaus were observed in both discharging/charging for all three cells at all C-rates. At 0.2, 0.25, 1 and 1.5 C, discharge capacities were 497, 284, 171 and 110 mAh g^{-1} for GF cell, 898, 591, 428 and 340 mAh g^{-1} for PCGF cell and 906, 674, 493 and 362 mAh g^{-1} for ACGF cell, respectively. These results indicated that the increase in current density resulted in decreased specific capacity for all three cells. Furthermore, the specific capacities of the ACGF cell at all current densities were higher than those of the PCGF cell, which was due to the porous structure and the oxygen containing groups of the AC, trapping more polysulfides from shuttling compared to bare GF and PC GF.

To further understand the electrochemical behaviour of GF, PCGF and ACGF cells, electrochemical impedance spectroscopy analysis was employed to obtain Nyquist plots at an open circuit

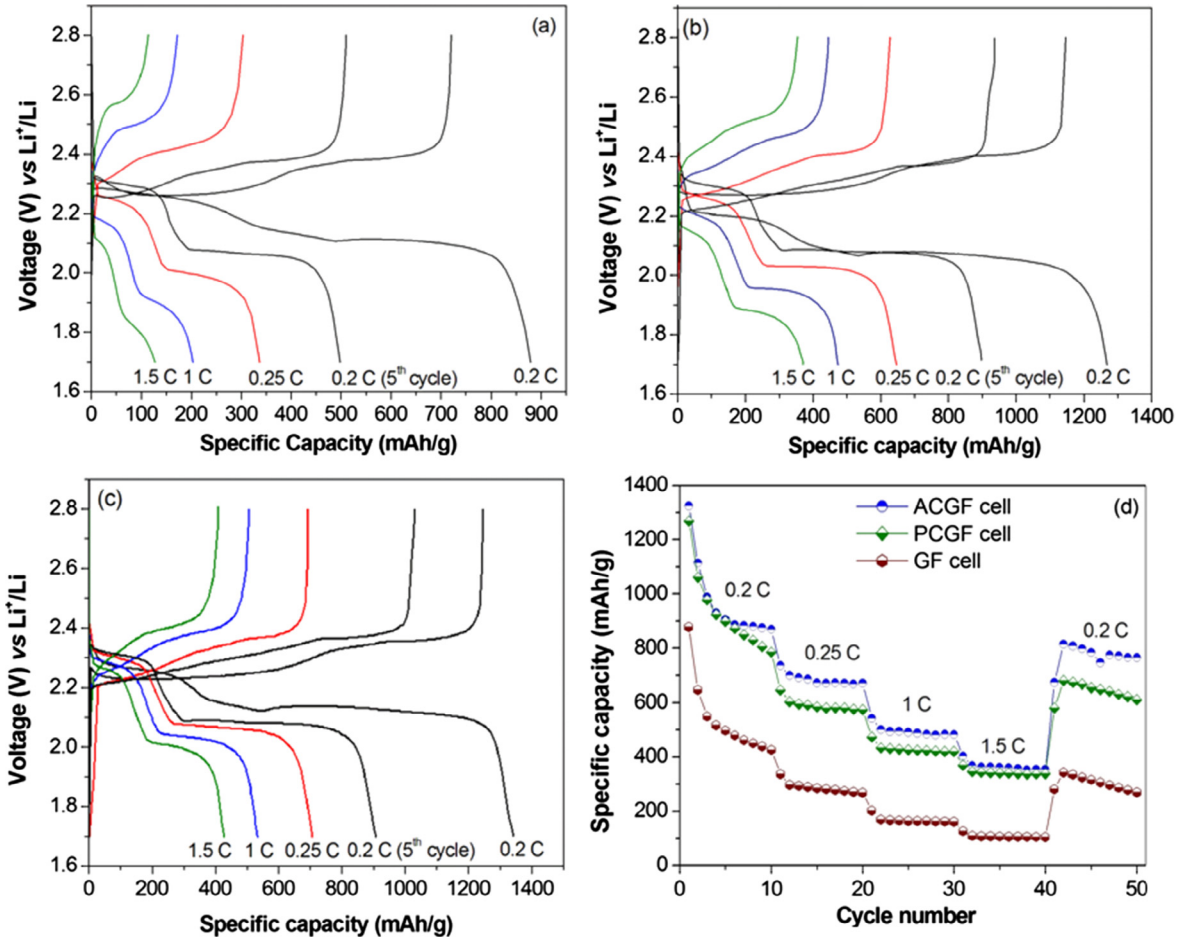

Fig. 7. Galvanostatic charge-discharge curves at different C-rates for (a) GF, (b) PC and (c) AC cells and (d) rate capabilities of GF, PC and AC cells.

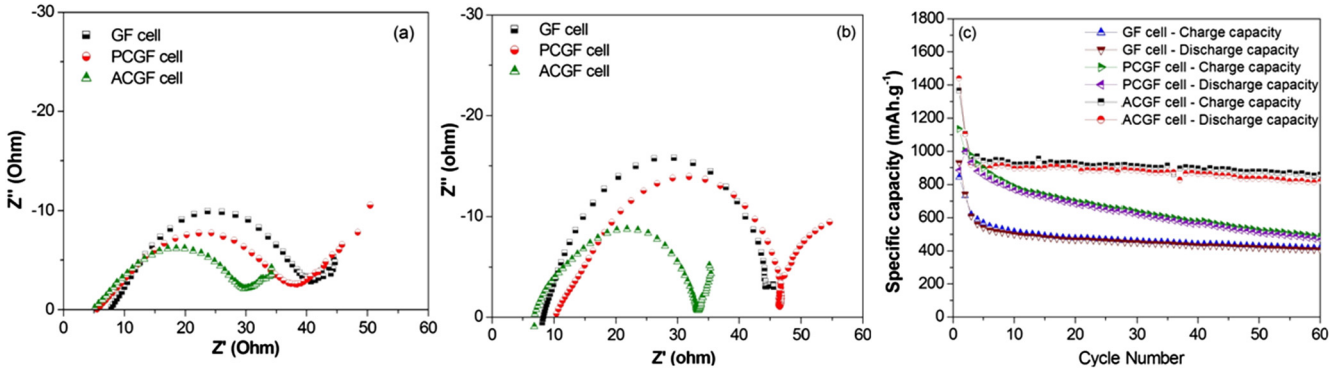

Fig. 8. EIS spectra of GF, PCGF and ACGF cells (a) before and (b) after cycling. (c) Cycling stability curve of all the cells.

potential both before and after cycling (Fig. 8a, b). All three cells exhibited a single depressed semicircle at high frequency (HF) region and an inclined line at low-frequency region. The depressed semicircle in the HF region represented the charge transfer resistance (R_{ct}) of the cells. On the other hand, the inclined line was the evidence of Li-ion diffusion and so-called Warburg diffusion. Depressed semicircle intercepts at a real axis of HF region gave the solution resistance (R_s) or (R_{ESR}), which was composed of the internal resistance of the electrode, the interfacial resistance of the active materials and substrate and an ionic resistance of the electrolyte [53,54]. In Fig. 8a, the experimental Nyquist plots were fitted with an equivalent circuit model using the Z-fit software before cycling and the calculated R_s values were 7.9, 5.4, and 4.9 Ohm for GF, PCGF and ACGF cells, respectively. The calculated R_{ct} values were 35.3, 33.3, and 25.7 Ohm for GF, PCGF and ACGF cells, respectively. It is clearly seen that the R_s of GF cell is higher than those of PCGF and ACGF cells. The reduction in R_s and R_{ct} of ACGF was due to the porous carbon coating, which could serve as a second current collector to minimize the internal resistance and at the same time could help inhibit the polysulfide diffusion and increase the active material utilization. These results are consistent with the CV data shown in Fig. 6c. Particularly, ACGF showed the lowest R_{ct} value due to the porous structure and high surface area of the KOH activated carbon (AC) [1]. Similarly, after cycling, the calculated R_{ct} values are 36.08, 36.14, and 26.48 Ω for GF, PCGF and ACGF cells separators, respectively (Fig. 8b).

Fig. 8c shows the cycling performance of GF, PCGF and ACGF cells at a current density of 0.2 C for over 60 cycles. At the first cycle, GF, PCGF and ACGF cells delivered specific capacities of 878, 1271 and 1321 mAh g^{-1}, respectively. It is seen that the ACGF cell shows higher capacity than other two cells with GF and PCGF, because of the high surface area and porosity of AC, which helps to trap polysulfides and provide more conductive sites for the reutilization of active material. Similarly, at the second cycle, the capacities were 645, 1065 and 1112 mAh g^{-1} for GF, PCGF and ACGF cells, respectively. Furthermore, during the ongoing cycles, different degrees of capacity decay occurred since the active sulfur cathode tended to form a steady state electrochemical reaction due to the high solubility of the polysulfide intermediates in the liquid electrolyte [55]. Accordingly, GF and PCGF cells showed the capacity retention of 56 and 51%, respectively at the end of the 50th cycle due to the combined effects of rapid irreversible loss of active material (due to shuttling phenomenon) and the formation of solid electrolyte interface (SEI) [55]. On the other hand, ACGF cell showed much better cycling stability (75% at 50th cycle) than other two cells due to the trapping of lithium polysulfides during the discharge process [16].

4. Conclusions

The present study reported biomass-derived porous carbon coated glass fiber separator for polysulfide inhibition in Li-S cells. As-prepared porous carbons with and without KOH activation were investigated in terms of structural and chemical characterization. The *R* factor value calculated from XRD revealed that more single-layer graphene sheets with the lower degree of graphitization were formed in AC. The redox peaks of PC and AC cells, sustaining their shape and position during cycling, demonstrated the better reversibility. At the first cycle, a high capacity of 1321 mAh g^{-1} was obtained for ACGF cell, which was higher than those of GF and PCGF cells (878 and 1271 mAh g^{-1}, respectively). Furthermore, the polarization potentials of the GF, PCGF and ACGF cells were 198, 178, and 71 mV, respectively. The decreased overpotential of ACGF cell shows the better reversibility resulted in trapping polysulfides during discharging. At 0.2 C the discharge capacity of the ACGF cell was 906 mAh g^{-1}, which was higher than those of PCGF (898 mAh g^{-1}) and GF (497 mAh g^{-1}) cells. On the other hand, ACGF cell delivered a high capacity of 786 mAh g^{-1} when the current density was lowered back to 0.2 C, retaining 86% of their initial capacities. Hence, KOH activated carbon coated GF separator (AC) is a promising material for polysulfide inhibition in Li-S batteries.

Acknowledgement

We would like to thank the University Grants Commission (UGC), India, for awarding **R. Kalai Selvan** the **Raman Post Doctoral Fellowship**. We also acknowledge the Ministry of Science, ICT and Future Planning of South Korea for providing Yun Sung Lee with a National Research Foundation of Korea (NRF) grant (No. 2016R1A4A1012224). This work was performed in part at the Analytical Instrumentation Facility (AIF) at North Carolina State University.

References

[1] J. Zhu, C. Chen, Y. Lu, J. Zang, M. Jiang, D. Kim, X. Zhang, Highly porous polyacrylonitrile/graphene oxide membrane separator exhibiting excellent anti-self-discharge feature for high-performance lithium–sulfur batteries, Carbon 101 (2016) 272–280.
[2] F. Zeng, Z. Jin, K. Yuan, S. Liu, X. Cheng, A. Wang, W. Wang, Y.S. Yang, High performance lithium–sulfur batteries with a permselective sulfonated acetylene black modified separator, J. Mater. Chem. A 4 (2016) 12319–12327.
[3] L.Q. Mai, A. Minhas-Khan, X. Tian, K.M. Hercule, Y.L. Zhao, X. Lin, X. Xu, Synergistic interaction between redox-active electrolyte and binder-free functionalized carbon for ultrahigh supercapacitor performance, Nat. Commun. 4 (2013) 2916–2923.

[4] J. Lim, J. Pyun, K. Char, Recent approaches for the direct use of elemental sulfur in the synthesis and processing of advanced materials, Angew. Chem. Int. Ed. 54 (2015) 3249–3258.
[5] S. Imtiaz, J. Zhang, Z.A. Zafar, S. Ji, T. Huang, J.A. Anderson, Z. Zhang, Y. Huang, Biomass-derived nanostructured porous carbons for lithium-sulfur batteries, Sci. China Mater. 59 (2016) 389–407.
[6] M. Yu, R. Li, M. Wu, G. Shi, Graphene materials for lithium–sulfur batteries, Energy Storage Mater. 1 (2015) 51–73.
[7] A. Manthiram, Y. Fu, S.H. Chung, C. Zu, Y.S. Su, Rechargeable lithium-sulfur batteries, Chem. Rev. 114 (2014) 11751–11787.
[8] R.C. Massé1, E. Uchaker, G. Cao, Beyond Li-ion: electrode materials for sodium- and magnesium-ion batteries, Sci. China Mater. 58 (2015) 715–766.
[9] J.S. Lee, J. Jun, J. Jang, A. Manthiram, Sulfur-immobilized, activated porous carbon nanotubes composites based cathodes for lithium –sulfur batteries, Small 160 (2017) 1602984–1602990.
[10] Y. Jiang, F. Chen, Y. Gao, Y. Wang, S. Wang, Q. Gao, Z. Jiao, B. Zhao, Z. Chen, Inhibiting the shuttle effect of Li–S battery with a graphene oxide coating separator: performance improvement and mechanism study, J. Power Sources 342 (2017) 929–938.
[11] M. Yu, A. Wang, F. Tian, H. Song, Y. Wang, C. Li, J.D. Hong, G. Shi, Dual-protection of a graphene-sulfur composite by a compact graphene skin and an atomic layer deposited oxide coating for a lithium-sulfur battery, Nanoscale 7 (2015) 5292–5298.
[12] H.B. Wu, S. Wei, L. Zhang, R. Xu, H.H. Hng, X.W. Lou, Embedding sulfur in MOF-derived microporous carbon polyhedrons for lithium-sulfur batteries, Chem. Eur. J. 19 (2013) 10804–10808.
[13] Z. Wang, Y. Dong, H. Li, Z. Zhao, H.B. Wu, C. Hao, S. Liu, J. Qiu, X. Wen Lou, Enhancing lithium–sulfur battery performance by strongly binding the discharge products on amino functionalized reduced graphene oxide, Nat. Commun. 5 (2014) 5002.
[14] H. Li, Y. Gong, C. Fu, H. Zhou, W. Yang, M. Guo, M. Li, Y. Kuang, A novel method to prepare a nanotubes@mesoporous carbon composite material based on waste biomass and its electrochemical performance, J. Mater. Chem. A 5 (2017) 3875–3887.
[15] J. Zhu, M. Yanilmaza, K. Fua, C. Chen, Y. Lu, Y. Ge, D. Kim, X. Zhang, Understanding glass fiber membrane used as a novel separator for lithium–sulfur batteries, J. Membr. Sci. 504 (2016) 89–96.
[16] A. Abbas, M.A. Ibrahem, L.H. Hu, C.N. Lin, J. Fang, K.M. Boopathi, P.C. Wang, L.J. Li, C.W. Chu, Bifunctional separator as a polysulfide mediator for highly stable Li–S batteries, J. Mater. Chem. A. 4 (2016) 9661–9669.
[17] J.-Z. Wang, L. Lu, M. Choucair, J.A. Stride, X. Xu, H.-K. Liu, Sulfur graphene composite for rechargeable lithium batteries, J. Power Sources 196 (2011) 7030–7034.
[18] Y. Yang, G. Zheng, Yi Cui, Nanostructured sulfur cathodes, Chem. Soc. Rev. 42 (2013) 3018–3032.
[19] N. Moreno, A. Caballero, L. Hernán, J. Morales, Lithium–sulfur batteries with activated carbons derived from olive stones, Carbon 70 (2014) 241–248.
[20] J. Sun, Y. Sun, M. Pasta, G. Zhou, Y. Li, W. Liu, F. Xiong, Y. Cui, Entrapment of polysulfides by a black phosphorus modified separator for lithium-sulfur batteries, Adv. Mater. 28 (2016) 9797–9803.
[21] G. Zhou, L. Li, D.W. Wang, X. Shan, S. Pei, F. Li, H.M. Cheng, A flexible sulfur graphene polypropylene separator integrated electrode for advanced Li–S batteries, Adv. Mater. 27 (2015) 641–647.
[22] S.H. Chung, A. Manthiram, High performance Li–S batteries with an ultra light weight MWCNT coated separator, J. Phys. Chem. Lett. 5 (2014) 1978–1983.
[23] L. Wang, J. Liu, S. Haller, Y. Wang, Y. Xia, A scalable hybrid separator for a high performance lithium-sulfur battery, Chem. Commun. 51 (2015) 6996–6999.
[24] G. Wang, Y. Lai, Z. Zhang, J. Li, Z. Zhang, Enhanced rate capability and cycle stability of lithium–sulfur batteries with a bifunctional MCNT@PEG-modified separator, J. Mater. Chem. A 3 (2015) 7139–7144.
[25] X. Qiana, L. Jin, D. Zhao, X. Yang, S. Wang, X. Shen, D. Rao, S. Yao, Y. Zhou, X. Xi, Ketjen black-MnO composite coated separator for high performance, rechargeable lithium-sulfur battery, Electrochim. Acta 192 (2016) 346–356.
[26] X. Qian, D.I. Zhao, L. Jin, S. Yao, D. Rao, X. Shen, Y. Zhou, X. Xi, A separator modified by spray-dried hollow spherical cerium oxide and its application in lithium sulfur batteries, RSC Adv. 6 (2016) 114989–114996.
[27] J. Zhang, J. Xiang, Z. Dong, Y. Liu, Y. Wu, C. Xu, G. Du, Biomass derived activated carbon with 3D connected architecture for rechargeable lithium – sulfur batteries, Electrochim. Acta 116 (2014) 146–151.
[28] H.S. Ryu, J.W. Park, J. Park, J.-P. Ahn, K.-W. Kim, J.-H. Ahn, T.-H. Nam, G. Wang, H.-J. Ahn, High capacity cathode materials for Li-S batteries, J. Mater. Chem. A 1 (2013) 1573–1578.
[29] W. Yi, Z. Huaiyu, H. Jian, L. Yun, Z. Shushu, Wetlaid nonwoven fabric for separator of lithium ion battery, J. Power Sources 189 (2009) 616–619.
[30] H. Wei, J. Ma, B. Li, Y. Zuo, D. Xia, Enhanced cycle performance of lithium-sulfur batteries using a separator modified with a PVDF-C layer, ACS Appl. Mater. Interfaces 22 (2014) 20276–20281.
[31] J. Huang, T.Z. Zhuang, Q. Zhang, H. Peng, C.M. Chen, F. Wei, Permselective graphene oxide membrane for highly stable and antiself discharge lithium-sulfur batteries, ACS Nano 9 (2015) 3002–3011.
[32] Z. Yang, Y. Xia, R. Mokaya, Enhanced hydrogen storage capacity of high surface area zeolite-like carbon materials, J. Am. Chem. Soc. 129 (2007) 1673–1679.
[33] S.T. Senthilkumar, R. Kalai Selvan, N. Ponpandian, J.S. Melo, Y.S. Lee, Improved performance of electric double layer capacitor using redox additive (VO^{2+}/VO^{2+}) aqueous electrolyte, J. Mater. Chem. A 1 (2013) 7913–7919.
[34] B.E. Warren, X-ray diffraction in random layer lattices, Phys. Rev. 9 (1941) 693–698.
[35] B.S. Girgis, Y.M. Temerk, M.M. Gadelra, I.D. Abdullah, X-ray diffraction patterns of activated carbons prepared under various conditions, Carbon Sci. 8 (2007) 95–100.
[36] Y. Liu, J.S. Xue, T. Zheng, J.R. Dahn, Mechanism of lithium insertion in hard carbons prepared by pyrolysis of epoxy resins, Carbon 34 (1996) 193–200.
[37] A. Guinier, Smull-Angle Scattering of X-rays, Wiley and Sons, New York, 1955.
[38] D. Qu, Investigation of hydrogen physisorption active sites on the surface of porous carbonaceous materials, Chem. Eur. J. 14 (2008) 1040–1046.
[39] S.T.S. Kumar, B.S. Kumar, S. Balaji, C. Sanjeeviraja, R.K. Selvan, Preparation of activated carbon from sorghum pith and its structural and electrochemical properties, Mater. Res. Bull. 46 (2011) 413–419.
[40] J. Robertson, Hard amorphous (diamond-like) carbons, Prog. Solid State Chem. 21 (1999) 199–333.
[41] A. Janes, H. Kurig, E. Lust, Characterisation of activated nanoporous carbon for supercapacitor electrode materials, Carbon 45 (2007) 1226–1233.
[42] M. Thommes, K. Kaneko, A.V. Neimark, J.P. Olivier, F. Rodriguez-Reinoso, J. Rouquerol, K.S.W. Sing, Physisorption of gases, with special referenceto the evaluation of surface area and pore size distribution (IUPAC technical report), Pure Appl. Chem. 87 (2015) 1051–1069.
[43] W. Huang, H. Zhang, Y. Huang, W. Wang, S. Wei, Hierarchical porous carbon obtained from animal bone and evaluation in electric double-layer capacitors, Carbon 49 (2011) 838–843.
[44] E.P. Barrett, L.G. Joyner, P.P. Halenda, The determination of pore volume and area distributions in porous substances. I. Computations from nitrogen isotherms, the volume and area distributions in porous substances, J Am. Chem. Soc. 73 (1951) 373–380.
[45] M. Inagaki, Pores in carbon materials-importance of their control, New Carbon Mater. 24 (2009) 193–232.
[46] S.T. Senthilkumar, R. Kalai Selvan, J.S. Melo, C. Sanjeeviraja, High performance solid-state electric double layer capacitor from redox mediated gel polymer electrolyte and renewable tamarind fruit shell derived porous carbon, ACS Appl. Mater. Interfaces 5 (2013) 10541–10550.
[47] W. Xing, C.C. Huang, S.P. Zhuo, X. Yuan, G.Q. Wang, D.H. Jurcakova, Z.F. Yan, G. Q. Lu, Hierarchical porous carbons with high performance for supercapacitor electrodes, Carbon 47 (2009) 1715–1722.
[48] W. Shen, T. Hu, W. Fan, Cellulose generated-microporous carbon nanosheets with nitrogen doping, RSC Adv. 4 (2014) 9126–9132.
[49] K. Yang, Q. Gao, Y. Tan, W. Tian, W. Qian, L. Zhu, C. Yang, Biomass-derived porous carbon with micropores and small mesopores for high-performance lithium-sulfur batteries, Chem. Eur. J. 22 (2016) 3239–3244.
[50] J. Zhu, Y. Ge, D. Kim, Y. Lu, C. Chen, M. Jiang, X. Zhang, A novel separator coated by carbon for achieving exceptional high performance, Nano Energy 20 (2016) 176–184.
[51] D. Zhao, X. Qian, L. Jin, X. Yang, S. Wang, X. Shen, S. Yao, D. Rao, Y. Zhou, X. Xi, Separator modified by Ketjen black for enhanced electrochemical performance of lithium–sulfur batteries, RSC Adv. 6 (2016) 13680–13685.
[52] M. Xiang, Y. Wang, J. Wu, Y. Guo, H. Wu, Y. Zhang, H. Liu, Natural silk cocoon derived nitrogen-doped porous carbon nanosheets for high performance lithium-sulfur batteries, Electrochim. Acta 227 (2017) 7–16.
[53] W. Lin, Y. Chen, P. Li, J. He, Y. Zhao, Z. Wang, J. Liu, F. Qi, B. Zheng, J. Zhou, C. Xu, F. Fu, Enhanced performance of lithium sulfur battery with a reduced graphene oxide coating separator, J. Electrochem. Soc. 162 (2015) A1624–A1629.
[54] Z. Deng, Z. Zhang, Y. Lai, J. Liu, J. Li, Y. Liu, Electrochemical impedance spectroscopy study of a lithium/sulfur battery: modeling and analysis of capacity fading, J. Electrochem. Soc. 160 (2013) A553–A558.
[55] Y.S. Su, A. Manthiram, A new approach to improve cycle performance of rechargeable lithium-sulfur batteries by inserting a free-standing MWCNT interlayer, Nat. Commun. 3 (2012) 542–555.